J. Fluid Mech. (1999), *vol.* 389, *pp.* 209–228. Printed in the United Kingdom

Investigation of thermocapillary convection in a three-liquid-layer system

By Ph. GÉORIS[1], M. HENNENBERG[1], G. LEBON[2] AND J. C. LEGROS[1]

[1] Université Libre de Bruxelles, Service de Chimie Physique EP, CP165-62, 50 Av F. D. Roosevelt 1050, Brussels, Belgium
[2] Université de Liège, Institut de Physique B5 Sart Tilman, B 4000 Liège 1, Belgium

(Received 6 March 1997 and in revised form 7 January 1999)

This paper presents the first experimental results on Marangoni–Bénard instability in a symmetrical three-layer system. A pure thermocapillary phenomenon has been observed by performing the experiment in a microgravity environment where buoyancy forces can be neglected. This configuration enables the hydrodynamic stability of two identical liquid–liquid interfaces subjected to a normal gradient of temperature to be studied. The flow is driven by one interface only and obeys the criterion based on the heat diffusivity ratio proposed by Scriven & Sternling (1959) and Smith (1966). The measured critical temperature difference for the onset of convection is compared to the value obtained from two-dimensional numerical simulations. The results of the simulations are in reasonable agreement with the velocimetry and the thermal experimental data for moderate supercriticality. Numerically and experimentally, the convective pattern exhibits a transition between different convective regimes for similar temperature gradients. Their common detailed features are discussed.

1. Introduction

Since the works by Block (1956) and Pearson (1958), surface tension gradient is known to be responsible for cellular convective instability in liquid layers bounded by a gas phase and heated from the opposite rigid boundary side. These thermocapillary instabilities occur even in the absence of gravity.

Pearson introduced a dimensionless number, the Marangoni number Ma, which expresses the ratio of the surface tension force to viscous and thermal dissipations:

$$Ma = \frac{(\mathrm{d}\sigma/\mathrm{d}T)h\Delta T}{\kappa\,\mu}, \tag{1.1}$$

where κ, μ and h are the thermal diffusivity of the liquid, the dynamic viscosity and the thickness of the layer respectively, $\mathrm{d}\sigma/\mathrm{d}T$ is the interfacial tension variation with the temperature and $\Delta T = T_{hot} - T_{cold}$ is the temperature difference imposed across the layer. Pearson considered a single layer of liquid, ignoring the presence of the gas phase; he showed that the instability results from the amplification of velocity perturbations induced by surface tension gradients competing with the thermal and momentum diffusions.

In a double-layer configuration, the convective motions in both bulk regions will contribute positively or negatively to the growth of interfacial tension gradients.

The theoretical work of Scriven & Sternling (1959) is the first investigation of the Marangoni–Bénard instability in superposed layers. Unlike previous works, Scriven & Sternling treated the problem of the mass transfer of a tensioactive solute across the interface as an hydrodynamic instability. They considered two infinite layers in contact with each other and disregarded mass accumulation along the interface so that their conclusions also apply to heat transfer, provided the heat diffusivity is replaced by a mass diffusion coefficient. They proposed a criterion for the occurrence of the vigorous agitation phenomenon sometimes observed near the interface of two superposed non-equilibrated organic liquid phases.

They concluded the following: for a definite direction of the transfer of the surface-active agent, the parameters determining whether solutal instability will take place or not are the ratio of the diffusion coefficients in the two phases and the ratio of the kinematic viscosity of both liquid phases adjacent to the interface. But these authors did not provide a critical value of the Marangoni number.

The pioneering work of Scriven & Sternling was extended by Smith (1966) and Reichenbach & Linde (1981). Smith treated the case of two superposed immiscible liquid layers of finite depth subjected to a temperature gradient. The possible interfacial deformations were included which introduced the weight of the displaced liquid. The analysis was restricted to neutrally stable modes (no overstability) and he obtained a general analytical expression for the marginal Marangoni number. If deformations of the interface are disregarded, the sign of the marginal Marangoni number, which corresponds to the sign of the temperature gradient, is governed only by the ratio of the heat diffusivities of the liquid phases.

Reichenbach & Linde made an extensive analysis of the problem investigated by Smith, as they extended his systematic study to all possible marginal cases, neutral ones as well as overstable ones. However, the numerical resources available at that time lead to conclusions for overstability less global than for neutral stability cases.

Later, Zeren & Reynolds (1972) studied experimentally and theoretically the same configuration as Smith, neglecting the possibility of critical overstable modes. They considered the particular system of benzene over water because its parameters allow the existence of instability when heating from the upper or the lower side. They failed to observe pure thermocapillary instability when heating from above; this was attributed to an interfacial contamination.

Imaishi & Fujinawa (1974) took up Zeren & Reynolds' investigation. They were able to measure the critical temperature difference for the onset of combined buoyancy- and thermocapillary-driven instability in clean and contaminated two layer systems (water–carbon tetrachloride and benzene–water systems) heated from below. Their measurements largely confirm the results of the linear stability analysis but practical difficulties prevented them from detecting the instability in systems heated from above and observing the flow pattern.

Since 1974, as far as we know, no experimental results on the Marangoni–Bénard instability in a multilayered system have been published, while there exists a vast theoretical and numerical literature on the two-layer Rayleigh–Bénard problem (see e.g. Rasenat, Busse & Rehberg 1989 and Cardin, Nataf & Dewost 1991). Wahal & Bose (1988) extended the discussion to a case where the top layer is bounded by a free surface containing an insoluble surface-active agent. However, they considered the particular case of two fluids of very similar properties, so that an experimental verification is very difficult. More recently, Simanovskii & Nempomyashchy (1993) addressed numerically and theoretically some of the most interesting aspects of the two layer Rayleigh and Marangoni–Bénard instability.

As a forerunner of the present work, Géoris *et al.* (1993) discussed a model of a symmetrical three-layer configuration where one fluid is sandwiched between two layers of another fluid. This is a situation that microgravity could make realistic. The linear stability analysis is supplemented by numerical computations on systems of experimental interest. As already found by Smith for the two-layer configuration, the driving interface for the monotonic (non-oscillatory) case, is selected by the ratio of the heat diffusivities of the liquids. The viscosity ratio does not influence the nature (monotonic or oscillatory) of the critical convective mode because of symmetry. When the heat diffusivities tend to be equal, the monotonic convection modes are restricted to large wavenumbers and are replaced by an oscillatory mode with a critical wavenumber about 2.

The present paper reports first experimental results on pure thermocapillary instability in a multilayer system, to fill the void separating theory from experiment. The thermocapillary instability of the multilayer system depicted in figure 1 is studied in a real microgravity environment. The hottest and coldest layers are labelled 1 and 3, respectively. Apart from the difference in temperature, these outer layers are identical in every other aspects. The middle layer, labelled 2, is a different immiscible liquid. In this particular set-up, the free interfaces 1-2 and 1-3 are identical. In microgravity, such a symmetric situation can be made stable with respect to the Rayleigh–Taylor instability, provided some precautions are taken in the design of the experimental hardware.

The paper is organized as follows. In the next section, the experimental set-up, conditions and fluid properties are described. Then, the results of the linear stability analysis and the numerical simulations are presented for the configuration corresponding to the experiment. Finally, the results of the experiment are analysed and compared with the theoretical and numerical data.

2. Experiment description

The microgravity experiment was performed in June 1994 during the IML2 mission of Spacelab aboard the US Space Shuttle. The experiment was conducted in the BDPU (Bubble Drop and Particle Unit) as part of the programme developed by the European Space Agency. The BDPU is a multi-user facility designed to study fluid physics in microgravity. This instrument provides the thermal control and the flow visualization tools for a dedicated experimental cell.

2.1. *Fluids*

Fluorinert FC70 (3M) for the lateral layers and silicone oil 10 cSt (Dow Corning) for the central layer were selected for the experiment. The physical properties of the liquids and their relevant ratios are listed in table 1: $\mathrm{d}\sigma_{\mathrm{FC70-Si}}/\mathrm{d}T$ has been measured using the maximum drop weight method described by Harkins (1952), and the value obtained is in good agreement with the measurement by Burkersroda, Prakash & Koster (1994) using the de Noüy ring technique ($-2.9 \times 10^{-5}\,\mathrm{N\,m^{-1}\,K^{-1}}$).

2.2. *Fluid container*

The experimental set-up is represented in figure 1. The fluid container is made of a rectangular quartz frame closed on two sides by two sapphire windows, each being 1 cm thick. Each liquid layer is 8 mm thick, 50 mm wide and 35 mm deep. Initially, the layers are separated by two 50 μm thick stainless steel curtains to prevent mixing before the beginning of the experiment. The boundaries between the layers are kept

		Fluorinert FC70 (layers 1 and 3)	Silicone oil 10 cSt (layer 2)	(1)/(2)
Kinematic viscosity	$\nu(m^2\,s^{-1})$	13.4×10^{-6}	$9.08 \times 10^{-6}(35\,^{\circ}C)$	1.48
Dynamic viscosity	$\mu(kg\,m^{-1}s^{-1})$	2.55×10^{-2}	$8.40 \times 10^{-3}(35\,^{\circ}C)$	3.04
Heat conductivity	$\lambda(W\,m^{-1}\,K^{-1})$	7.00×10^{-2}	1.34×10^{-1}	0.522
Thermal diffusivity	$\kappa(m^2\,s^{-1})$	3.44×10^{-8}	9.51×10^{-8}	0.362
Density	$\rho(kg\,m^{-3})$	1940	934	2.08
Prandtl number	Pr	390	95	4.11
Surface tension	$\sigma(N\,m^{-1})$		6.9×10^{-3}	
	$d\sigma_{FC70-Si}/dT(N\,m^{-1}K^{-1})$		-2.7×10^{-5}	

TABLE 1. Physical properties of the liquids.

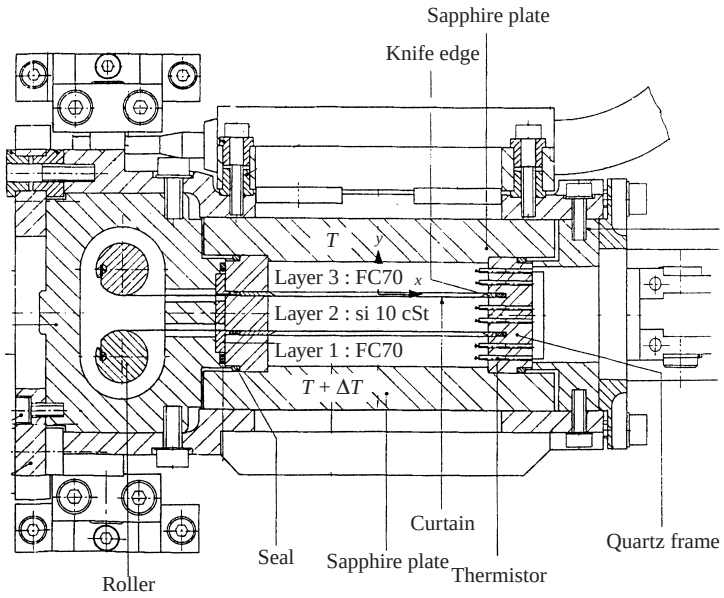

FIGURE 1. Symmetrical three-layer system and outline of the experimental set-up.

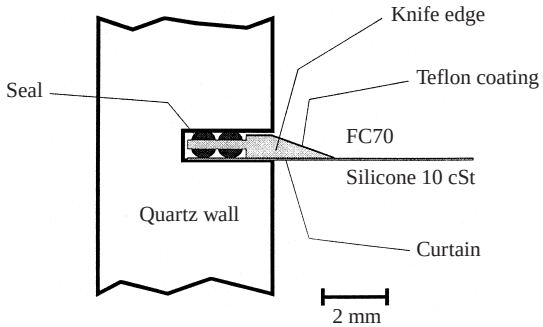

FIGURE 2. Close-up of the antiwetting knife edge. Teflon coating on the FC70 side ensures perfect anchorage of the layer edges.

leak tight by Viton seals moulded on an anti-wetting frame forming a knife edge as depicted in figure 2. Because the knife edge penetrates 2 mm into the fluid cell, the effective lengths of the free interfaces are 46 mm rather than 50 mm. At the beginning of the experiment, the curtains are pulled out and gently wound (0.25 mm s^{-1}) on the rollers (figure 1) creating two free liquid–liquid interfaces subjected to a Marangoni effect. Heating and cooling are achieved with electrical resistance and Peltier elements located along the edges of the sapphire windows.

2.3. *Stability of the three-layer configuration*

In microgravity, the static shapes of connected liquid phases are governed by the interfacial forces only. In the absence of walls, a three-layer configuration such as shown in figure 1 would be unstable. Indeed, the surface tension forces would act to minimize the surface with respect to the volume of the layers, curving the free interfaces and leading presumably to connected spherical phases. In a finite container, the situation is different because the layers will remain flat provided that their edges are properly anchored on the walls. Here, anchorage is achieved using two stainless steel frames coated on one side with a Teflon film (figure 2) that prevents creeping of the silicone oil along the quartz wall. Indeed, unlike quartz and stainless steel, Teflon is wetted preferentially by Fluorinert rather than by silicone oil. Thus the Teflon-coated sides of the frames are oriented towards the Fluorinert layers.

Beside controlling the wall wetting, the experimental set-up must be designed to satisfy another specific requirement: the interfacial tension has to counterbalance effectively the liquid density difference. This condition has to be fulfilled because of the low residual gravity level in the Space Shuttle.

In the simplified case of the Rayleigh–Taylor instability, the residual gravity being normal to the interfaces, the surface tension will stabilize the arrangement for sufficiently short wavelengths. The critical wavelength λ_m for the onset of the Rayleigh–Taylor instability for two liquids of infinite lateral extent is given by the capillary length (Chandrasekhar 1961, chap. X):

$$\lambda_m = 2\pi \left(\frac{\sigma}{g(\rho_2 - \rho_1)} \right)^{1/2}. \tag{2.1}$$

The maximum tolerable gravity level g^* can be estimated from (2.1) knowing that the 46 mm length of the free available surface has to be smaller than λ_m to exclude the appearance of the Rayleigh–Taylor instability. It is found that

$$g^* \approx 1.30\,10^{-2} g_0 \quad \text{where} \quad g_0 = 9.81\ \text{m s}^{-1}.$$

In the Space Shuttle, the mean microgravity level is lower than $10^{-4}\, g_0$. The Rayleigh–Taylor instability mechanism will be inactive for the present geometry and indeed has not been observed.

2.4. *Flow visualization*

The liquids are seeded with silver-coated ceramic spheres whose diameters range between 80 and 100 μm. The flow is visualized using a He-Ne laser light sheet oriented parallel to the longest side of the test container and located 10 mm from the front wall. To avoid sedimentation due to the residual acceleration, the densities of the particles match the densities of the liquids to within a few per cent.

k_c	Ma_c	ΔT_c^{FC70}(°C)	ΔT_c^{Tot}(°C)
1.965	500.78	2.03	5.13

TABLE 2. Results of the linear stability analysis.

3. Theoretical results

3.1. *Linear stability analysis*

The expression leading to the critical marginal Marangoni number for a symmetrical three-layer system of infinite lateral extent, of equal depths, and with flat interfaces was obtained analytically by Géoris *et al.* (1993) for the case of monotonic instability. Although the results of the linear stability analysis cannot strictly apply to a finite-size container, Dauby & Lebon (1996) showed that in the case of thermocapillary convection in a single layer, the confinement due to rigid walls exerts only a small stabilization for not too small aspect ratios. For instance, in a $L/h \times W/h = 6 \times 4$ rectangular box, $Ma_c = 84.4$ (instead of 79.6 for an infinite layer). In the present case with $L/h \times W/h = 6.25 \times 4.375$, the stabilizing effect due to the confinement is expected to be as small.

The thermal characteristics of the lateral walls, which are not taken into account in the linear analysis, introduce a new feature which is more important than the pure geometrical aspect due to confinement. Indeed, heat is transferred across the lateral borders and the large difference in thermal conductivity between the Fluorinert and the silicone oil (see table 1) acts together with the highly conductive quartz to induce a lateral gradient. In the present case, thus, a steady rest state cannot actually exist in the vicinity of the lateral walls. The effect of conducting lateral walls has to be modelled in the numerical analysis. The critical values derived from the previous linear stability analysis (Géoris *et al.* 1993) for an infinite lateral system are given in table 2. The properties of the FC70 are used as scaling units. The Marangoni number is

$$Ma = \frac{(-\mathrm{d}\sigma_{\mathrm{FC70-Si}}/\mathrm{d}T)h_{\mathrm{FC70}}\Delta T_{\mathrm{FC70}}}{\kappa_{\mathrm{FC70}}\mu_{\mathrm{FC70}}}.$$

Since the silicone oil used for the middle layer is five time less viscous (10 cSt instead of 50 cSt) than the previously considered one (Géoris *et al.* 1993), the critical Marangoni number is smaller. The critical wavenumbers for the two cases studied are very close to one another.

The horizontal component of the velocity at the marginal state and the corresponding two-dimensional flow pattern are shown in figures 3(*a*) and 3(*b*) respectively. The flow is driven by the hotter interface. The flow in the middle layer will drag the colder interface, creating a small vortex in the top layer. The colder interface is merely passive and only transmits shear.

The physical explanation is as follows. When a positive thermal disturbance in layer 1 reaches the 1-2 interface, it creates a hot spot and the interfacial tension gradient that results from it induces a flow that will amplify the initial disturbance. In layer 2, due to velocity continuity across the interface, the induced flow will bring colder fluid that damps the temperature gradient along the interface. It thus exerts a stabilizing effect on the system. In our case, the heat diffusivity of the middle layer (silicone oil) is about three times larger than that of the outer layers (Fluorinert FC70). Heat is transported by the flow more effectively in layer 1 so the destabilizing effect will

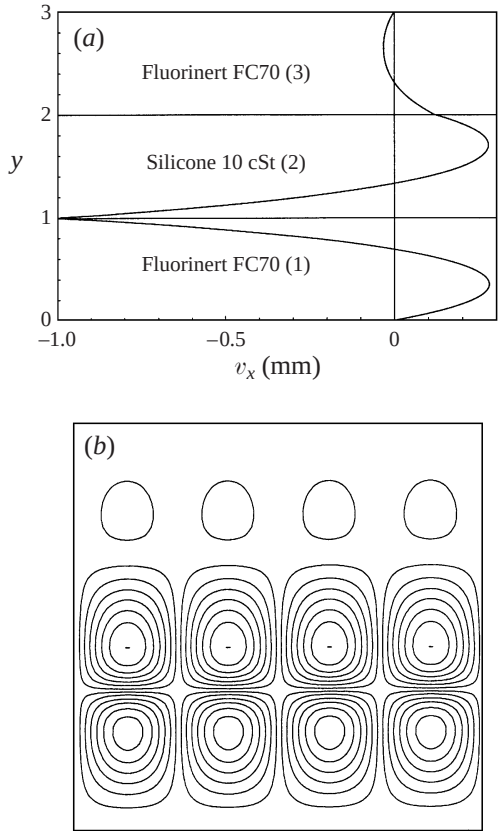

FIGURE 3. Linear stability analysis results. (*a*) Normalized horizontal velocity profile at the marginal state: $Ma = Ma_c$ and $k = k_c$. The flow is driven by the 1-2 interface. The 1-3 interface transmits only shear. (*b*) Streamlines at the marginal state.

predominate and the 1-2 interface will be active. The same reasoning, applied in a symmetrical way to the 2-3 interface, shows that it should be passive. When a hot spot reaches the 2-3 interface, the induced thermal gradient is damped by the corresponding downwards flow in layer 3 because of its lower heat diffusivity.

3.2. *Numerical simulations*

3.2.1. *Method*

The nonlinear Navier–Stokes and the energy equations are solved numerically in two-dimensions for the present set-up under zero gravity conditions. In each layer, the dimensionless balance laws of momentum and energy are expressed in terms of the stream function ψ and the vorticity function ϕ:

$$\partial_t \phi + \partial_y \psi \partial_x \phi - \partial_y \phi \partial_x \psi = \frac{\nu_l}{\nu_1} \Delta T, \tag{3.1}$$

$$Pr(\partial_t T + \partial_y \psi \partial_x T - \partial_y T \partial_x \psi) = \frac{\kappa_l}{\kappa_1} \Delta T, \tag{3.2}$$

where

$$\frac{\partial \psi}{\partial y} = v_x \quad \text{and} \quad -\frac{\partial \psi}{\partial x} = v_y, \tag{3.3}$$

$$\Delta \psi = \phi. \tag{3.4}$$

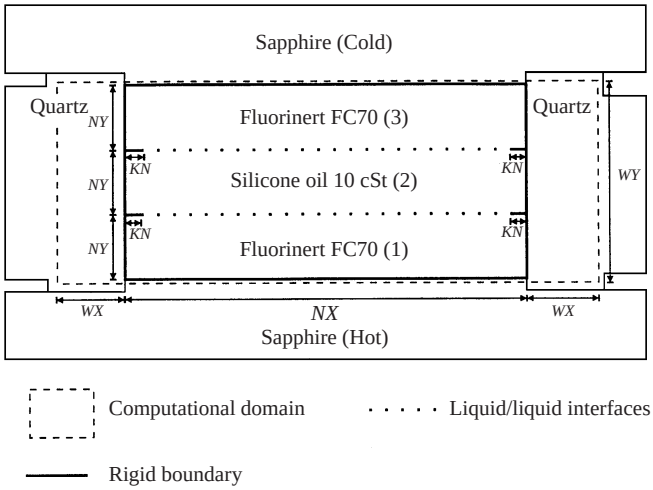

FIGURE 4. Grid organization for two-dimensional numerical simulations.

The equations are discretized on a uniform rectangular grid using the centred-difference technique and solved using the ADI scheme. The ADI scheme, of second-order accuracy in space, is more stable than the pure explicit scheme (Peyret & Taylor 1990) and is known to give the same results for multilayer convection (Simanovskii & Nepomnyashchy 1993). The Poisson equation (3.4) is solved using the over-relaxation technique.

The computational domain is divided into five parts: three for the liquids ($NX \times NY$) and two for the lateral quartz walls ($WX \times WY$) (see figure 4). In each of the five domains, nodes are identified by two coordinates (i, j). The index i varies along the x-axis from 1 to NX in the liquids and from 1 to WX in the lateral quartz walls. The index j varies along the y-axis from 1 to NY in the liquids and from 1 to WY in the lateral quartz walls. The highly conductive sapphire plates are represented by a single line of nodes kept at constant temperature. The knife edge is modelled using a single row (KN) of nodes where rigid boundary conditions apply. The Navier–Stokes, energy and Poisson equations are then solved for the internal nodes in each layer independently and the boundary conditions are applied to compute the values of vorticity and temperature on the boundary nodes.

3.2.2. *Boundary conditions*

For simplicity, the labels of the liquid domain will be either dropped or replaced by a and b when referring to coupling conditions across the interface a-b that separates the liquids a and b.

Rigid walls. Along the rigid walls, the stream function ψ is constant and its first-order derivatives are zero. From definitions (3.3)–(3.4), developing ψ near the walls in a Taylor series, one finds along the left vertical wall

$$\phi_{(1)(j)} = \frac{8\psi_{(2)(j)} - \psi_{(3)(j)}}{2\Delta x^2} \quad \text{where} \quad \Delta x = \frac{L/h}{NX - 1}$$

in each liquid layer.

Heat transfer through the interfaces. At the interface *a-b*, the temperature field is continuous and the heat flux is conserved. The second-order-accuracy expression for the temperature of the nodes located on the free surface is

$$T_{a/b(i)} = \frac{(\lambda_a/\lambda_b)(4T_{a(i)(NY_a-1)} - T_{a(i)(NY_a-2)}) + 4T_{b_{(i)(2)}} - T_{b(i)(3)}}{3(1+\lambda_a/\lambda_b)}$$

Free interfaces. The interfaces are assumed to remain flat, for two different reasons. First, the crispation number N_{Cr} is about 2×10^{-5}. As shown by Takashima (1981), for such a low crispation number the deflection of the interface can be disregarded. Secondly, the aspect ratio of the layers (L/h) is moderate: $L/h = 5.75$ taking 8 mm for the height of each layer and 46 mm for their width. Since each layer has to contain at least one vortex corresponding to half of the wavelength λ_W of the instability, the minimum wavenumber k_m permitted in the fluid cell is

$$k_m = \frac{2\pi}{\lambda_w} = 0.55 \quad \text{where} \quad \frac{\lambda_w}{2} = 5.75;$$

k_m is larger than the critical wavenumber of the instability induced by surface deformation described by Scriven & Sternling (1964). Thus, the instability induced by surface deformation is prevented from occurring in the actual experimental volume.

The expressions for the vorticity along the free interface are found from the equality of the horizontal velocities and the expression (3.5) of the Marangoni effect:

$$\phi_a - \frac{\mu_b}{\mu_a}\phi_b = \frac{Ma}{Pr}\left(\frac{\partial T}{\partial x}\right)_{a/b}, \tag{3.5}$$

$$\phi_{a(i)(NY_a)} = -\frac{Ma(\mu_1/\mu_a)}{Pr(1+\mu_b/\mu_a)}\frac{\left(T_{a(i+1)(NY_a)}\right) - T_{a(i-1)(NY_a)}\right)}{2\Delta x},$$

where

$$Ma = \frac{(-\mathrm{d}\sigma/\mathrm{d}T)\Delta T_1 h_l}{\kappa_1 \mu_l} \quad \text{and} \quad Pr = \frac{v_1}{\kappa_1}.$$

Heat losses through the quartz walls. The ambient temperature around the fluid cell is colder than the temperature of the cold flange. Although the fluid cell has been carefully designed, when the temperature of the hot flange is increased, a small part of the heat flux unavoidably escapes through the lateral quartz walls. The modelling of the heat transfer through the vertical boundaries of the quartz walls is based on a three-dimensional finite-element study performed by the hardware manufacturer. These simulations show a small lateral heat loss (ϕ) from the lateral quartz wall, estimated to be about 6 W m^{-2} K^{-1} ΔT. The boundary condition for the temperature on the external faces of the quartz walls is

$$T_{(wx)(j)} = \frac{(4T_{(wx-1)(j)} - T_{(wx-2)(j)} - 2\Delta x\phi/\lambda_{wall})}{3},$$

where ϕ is the non dimensional heat loss and λ_{wall} is the heat conductivity of the quartz wall.

3.2.3. *Convergence*

The steady-state flow patterns are computed in each layer on a 120×30 grid (see figure 4). The temperature field in the lateral walls is computed on a 24×88 grid.

NX	NY	$\lvert\psi\rvert_{max}(\times 10^3)$	$\lvert v_x\rvert_{max}(\mu\mathrm{m\,s^{-1}})$	$\lvert v_y\rvert_{max}(\mu\mathrm{m\,s^{-1}})$
60	15	5.306	59.4	24.4
80	20	5.172	60.3	24.9
120	30	5.09	62.2	24.5
160	40	5.07	63.1	24.3
350	60	5.04	64.1	24.6
500	70	5.07	64.3	24.6

TABLE 3. Results of the convergence test ($\Delta T^{\mathrm{num}} = 10\,^{\circ}\mathrm{C}$ or $Ma = 977.4$).

ΔT^{num} (°C)	Ma	$\lvert\psi\rvert_{max}(\times 10^3)$	$\lvert v_x\rvert_{max}(\mu\mathrm{m\,s^{-1}})$	$\lvert v_y\rvert_{max}(\mu\mathrm{m\,s^{-1}})$
2	195.5	0.901	10.1	3.96
4	391.0	1.89	18.8	7.84
6	586.0	3.26	29.5	12.6
8	781.9	3.88	47.0	18.5
15	1466	7.49	94.3	35.1
20	1955	9.49	120.0	42.7

TABLE 4. Numerical results obtained for increasing ΔT^{num}.

The convergence of the code has been tested with different grids by increasing NX and NY for $Ma = 977.4$, corresponding to a temperature difference between the hot and the cold flange of $\Delta T^{\mathrm{num}} = 10\,^{\circ}\mathrm{C}$. The results of the convergence tests are summarized in table 3. Since the uncertainty in the values of the physical parameters of the liquids is at least a few percents, the convergence obtained is sufficient. There is no need to include an artificial perturbation at the beginning of the simulation to induce a steady flow, because of the influence of the lateral conductive walls. Steady convective patterns are computed for discrete increments of the temperature of the hot side corresponding to increasing values of the Marangoni number. Under such conditions, the steady-state situation previously obtained serves as an initial condition for the temperature increments.

3.2.4. *Numerical results*

Numerical values for the maximum stream function, and horizontal and vertical velocities are given for different ΔT^{num} in table 4. Three steady flow regimes are observed (see figure 5): regime 1 reflects the wall-induced flow due to the lateral temperature gradients (see figure 5*a*), regime 2 corresponds to the onset of the Marangoni–Bénard instability influenced however by the wall effect (see figure 5*b*) and, after an unsteady transition zone (see figure 5*c*), regime 3 (figure 5*d*) where the rotation of the vortices is reversed and is no longer determined by the wall effect.

The wall-induced flow – regime 1 (*figure 5a*). The difference in the heat conductivities of the liquids and the quartz wall impose temperature gradients along the free surfaces. The horizontal temperature gradient along the 1-2 interface scaled by the vertical temperature gradient $\Delta T^{\mathrm{num}}/3h$ computed in the conductive situation ($Ma = 0$) is given in figure 6. Although the lateral gradient is large (up to 70% of the vertically imposed gradient) close to the wall, it does not propagate beyond a few mm in the liquids, away from the walls. It is mainly located in the knife edge region ($10\,\mathrm{mm} < x < 12\,\mathrm{mm}$) where the cell design forbids any thermocapillary convection.

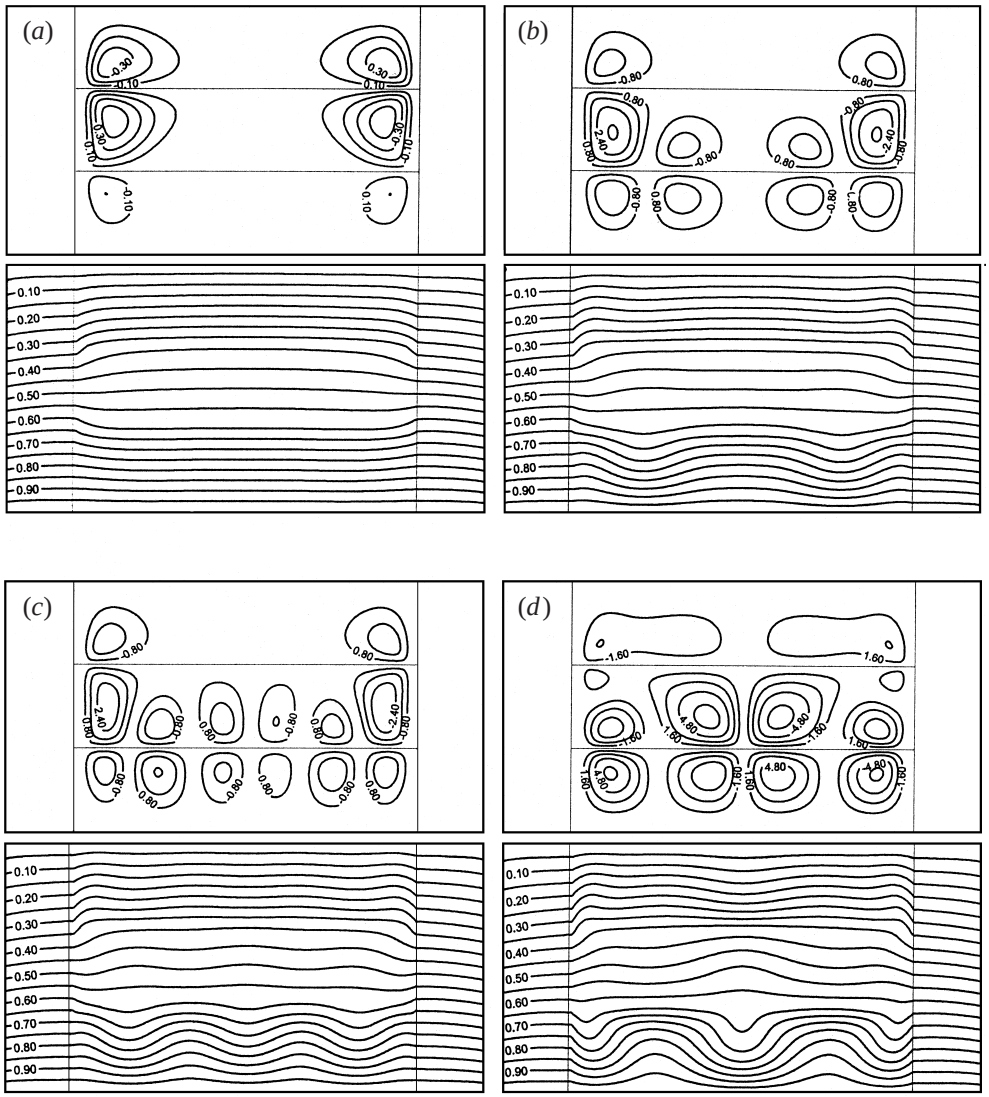

FIGURE 5. Streamlines ($\times 10^3$) and isotherms ($T/\Delta T^{\mathrm{num}}$) obtained by the two-dimensional numerical simulation. (*a*) $\Delta T^{\mathrm{num}} = 1.0\,^{\circ}\mathrm{C}$: wall-induced flow or regime 1 ($\psi_{\max} = 0.464 \times 10^{-3}$, $\psi_{\min} = -0.464 \times 10^{-3}$). (*b*) $\Delta T^{\mathrm{num}} = 6.0\,^{\circ}\mathrm{C}$: regime 2 ($\psi_{\max} = 3.27 \times 10^{-3}$, $\psi_{\min} = -3.27 \times 10^{-3}$). (*c*) $\Delta T^{\mathrm{num}} = 6.9\,^{\circ}\mathrm{C}$: transition between regimes 2 and 3 (unsteady) ($\psi_{\max} = 2.94 \times 10^{-3}$, $\psi_{\min} = -3.08 \times 10^{-3}$). (*d*) $\Delta T^{\mathrm{num}} = 14.0\,^{\circ}\mathrm{C}$: regime 3 ($\psi_{\max} = 7.03 \times 10^{-3}$, $\psi_{\min} = -7.03 \times 10^{-3}$). Positive values of the stream function correspond to anticlockwise rolls.

The effect of the lateral gradient is clearly visible on figure 5(*a*). Because of the symmetry of the arrangement, the temperature gradients along the free interfaces created by the walls have opposite signs. Consequently, near the walls, the 1-2 interface induces flow towards the centre of the cell whereas the 2-3 interface drives a flow towards the walls. The flow is very slow and no significant distortion of the isotherms from the state of rest can be observed.

Regime 2 (*figure 5b*). The existence of the wall-induced flow introduces a structural instability in the system (Drazin 1992, chap. 2). Thus, it is not obvious how to find the

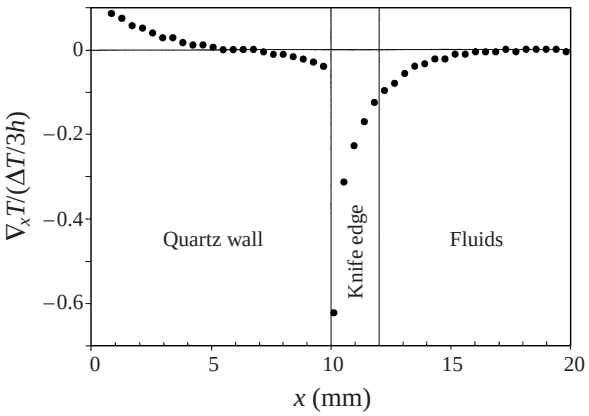

FIGURE 6. Horizontal temperature gradient scaled to the vertical temperature gradient across the quartz wall ($0 < x < 10\,\text{mm}$), along the knife edge ($10\,\text{mm} < x < 12\,\text{mm}$) and along the 1-2 interface ($x > 12\,\text{mm}$).

appropriate criterion defining the critical temperature difference ΔT_c^{num} for the onset of the Marangoni–Bénard convection. In an ideal situation where the lateral walls are perfectly insulating, ΔT_c^{num} is by definition the temperature difference at which departure from the rest conductive state is observed and the dynamic description of that case is clearly a pitchfork bifurcation (e.g. Dauby & Lebon 1996). But in the real experimental case, the weak wall-induced flow is superimposed on the Bénard–Marangoni instability onset. The bifurcation now contains an imperfection (Drazin 1992, chap. 2) and is described by the following Ginsburg–Landau equation for a single amplitude A (Manneville 1991):

$$\dot{A} = \gamma + \varepsilon A - \beta A^3 \quad \text{with} \quad \varepsilon = \Delta T - \Delta T_c. \tag{3.6}$$

The small parameter γ is a measure of the strength of the imposed imperfection. Indeed, $\gamma = 0$ corresponds to a perfect subcritical pitchfork perturbation. The strength of the lateral-wall-induced flow is proportional to ΔT in regime 1, so that we will assume that $\gamma = \zeta \Delta T$. β in equation (3.6) is a saturation parameter and is of no interest in the forthcoming discussion. The amplitude at the steady state is found from (3.6) which becomes

$$0 = \gamma + \varepsilon A - \beta A^3. \tag{3.7}$$

The steady amplitude A_s which corresponds to the imperfect bifurcation is the single root of the cubic equation (3.7) while the two other roots are complex conjugate when $\varepsilon < 0$. We have

$$A_s = \frac{F}{3(2)^{1/3}\beta} - \frac{2^{1/3}\varepsilon}{F}, \tag{3.8}$$

where

$$F = (27\beta^2\gamma + (729\beta^4\gamma^2 + 108\beta^2\varepsilon^3)^{1/2})^{1/3}.$$

If the dynamic of the system obeys the Ginsburg–Landau amplitude equation (3.6), the steady amplitude of the flow should obey (3.8).

In figure 7, values of the vertical component of velocity taken at $x = L/2$, $y = (2/3)h$, in layer 1 are plotted (circles) as a function of ΔT. At steady state, they define the amplitudes A. The unknown parameters β, ζ and ΔT_c^{num} will be determined

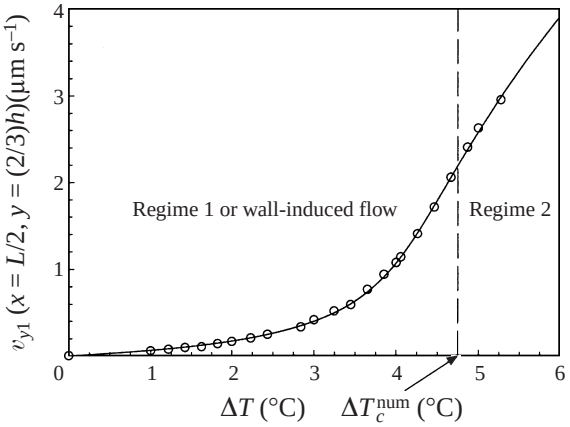

FIGURE 7. v_y in layer 1 taken at $(x = L/2, y = (2/3)h)$ (circles) plotted as a function of ΔT fitted with the real root of (3.7) (solid line). $\zeta = 0.23\,\mu\mathrm{m\,s^{-1}\,{}^\circ C^{-1}}$, $\beta = 0.11\,{}^\circ\mathrm{C}^{-1}(\mu\mathrm{m\,s^{-1}})^{-2}$ and $\Delta T_c^{\mathrm{num}} = 4.75\,{}^\circ\mathrm{C}$.

numerically by fitting (3.7) to figure 7. We obtain finally $\Delta T_c^{\mathrm{num}} = 4.75\,{}^\circ\mathrm{C}$. This value is in good agreement with the one obtained from linear stability analysis (see table 2).

As $\Delta T_c^{\mathrm{num}}$ is exceeded, the largely quiescent middle zone starts to move and two pairs of rolls appear in layers 1 and 2 (figure 5*b*). This pattern is highly reminiscent of the previous linear analysis results (figure 3*b*): the flow is driven by the 1-2 interface and layer 3 is almost at rest in the central region of the cell where the wall-induced flow will not propagate.

Transition between regimes 2 and 3 (*figure 5c*). Around $\Delta T^{\mathrm{num}} = 6.9\,{}^\circ\mathrm{C}$, the flow pattern undergoes a complex transformation. Two rolls appear in the central region of layers 1 and 2. This flow pattern shown on figure 5(*c*) is unsteady and its eventual stability range has not been investigated.

Regime 3 (*figure 5d*). The central rolls that appeared during the previous stage increase and compress the lateral rolls towards the walls. Finally, in layer 2, the lateral rolls are reduced to two very small vortices located close to the walls near the 2-3 interface. In layer 3, the convection consists of two wide vortices coupled with the central rolls of layer 2 and with the two small residual vortices.

This description of the flow pattern is valid over a wide range of thermal constraints. The structure of the flow remains qualitatively the same for ΔT^{num} up to 20 °C.

Velocity profiles. Three horizontal profiles of v_y in layer 1$(y = (2/3)\,h = 5.3\,\mathrm{mm})$ which are representative of the three different regimes are shown in figure 8. In regime 1 ($\Delta T^{\mathrm{num}} = 2.0\,{}^\circ\mathrm{C}$, squares), the flow is upward near the walls and is almost absent in the centre. Regime 2 ($\Delta T^{\mathrm{num}} = 6.6\,{}^\circ\mathrm{C}$, triangles) appears essentially as an amplification of the wall-induced flow. Fluid is upward near the walls and in the centre. In regime 3 ($\Delta T^{\mathrm{num}} = 9.7\,{}^\circ\mathrm{C}$, circles) the flow is in the opposite direction along the lateral walls. In the actual configuration, the situation where the flow is going downward along the lateral wall is preferred even though it is not favoured by the wall-induced thermal gradient. The reason why the thermocapillary effect tends to drive the interface flow towards the rigid conducting boundary rather than the reverse is still an open question. Nevertheless, the existence of a preferred direction is natural because the physical situations where the fluid moves away from the lateral walls or towards it are not identical.

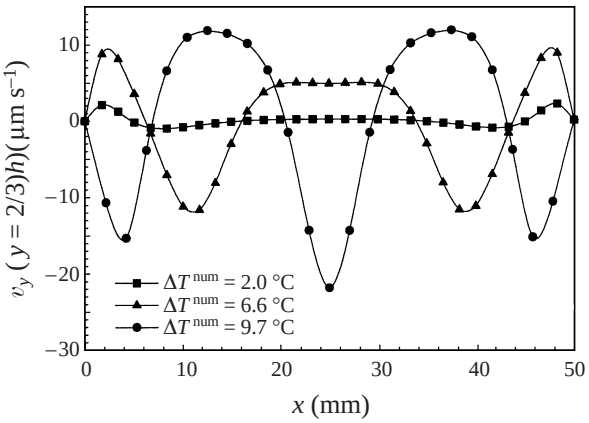

FIGURE 8. v_y in layer 1 at $y = (2/3)h$ plotted vs. x for the three different regimes.

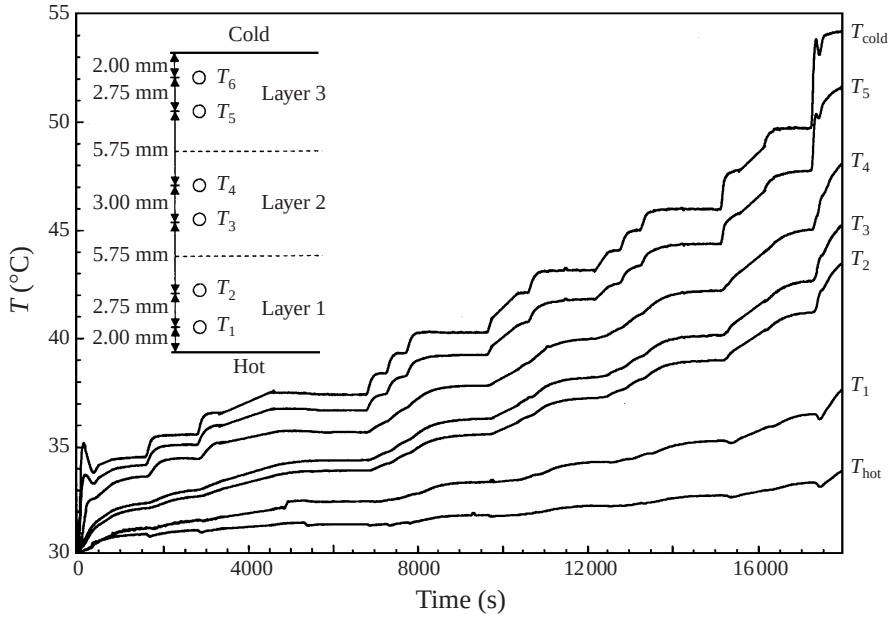

FIGURE 9. Thermistors positions and recordings during the whole duration of the experiment.

4. Analysis of the experimental results

4.1. *Thermal data*

Six thermistors, penetrating 5 mm into the liquid bulk, are inserted along the lateral wall of the quartz frame to record the temperatures near the lateral walls, throughout the experiment. The precise locations of these thermistors and the recording of the signals during the experiment are shown in figure 9. The instrumentation has to obey several external constraints such that, in order to change the temperature difference across the three-layer system, the reference point on the hot side is varied by jumps of one degree. The time span allowed for this experiment was rather short and it did not allow very accurate measurements of the critical temperature difference at the onset of convection.

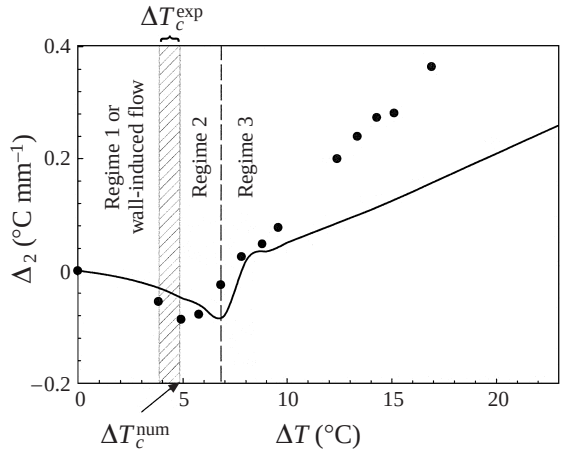

FIGURE 10. Comparison between experimental (circles) and numerical (solid line) values of Δ_2 at quasi-steady state.

For high Prandtl number fluids, beyond the onset of convection, the velocity field is slaved to the thermal field. The intensity of the flow will be reflected by the temperature recordings at the thermistors. From these signals, the results of the numerical simulations should be validated and thus the three different regimes identified (wall-induced flow, regime 2 and regime 3) depending on the temperature difference imposed between the two sapphire conductive plates. Since the distance between the thermistors above and beneath any *a-b* interface is 5.75 mm (figure 9), we define the following quantity Δ_2 from the thermistors signals to compare the temperature gradients across the interfaces:

$$\Delta_2 = \frac{T_4 - T_5}{5.75} - \frac{T_2 - T_3}{5.75}. \tag{4.1}$$

To compare experimental and numerical data, Δ_2 is plotted versus the temperature difference ΔT(ΔT^{exp} and ΔT^{num}) across the three layers (see figure 10). The general tendency is very similar for both the experimental and the numerical approaches. The reason for choosing (4.1) is that in regime 1, Δ_2 has to be close to zero because of the symmetry of the configuration and because the isotherms are not perturbed: $T_4 - T_5$ is more or less equal to $T_2 - T_3$ in the range of the imposed ΔT. When ΔT is increased, the hotter 1-2 interface pushes the liquids away from the walls, bringing hot Fluorinert and cold silicone oil to the 1-2 interfaces near the lateral wall. But in layer 3, the flow is very slow and the thermal field is undistorted from the conductive state. This means that $T_2 - T_3$ increases whereas $T_4 - T_5$ barely changes: consequently Δ_2 becomes negative. In the region $\Delta_2 < 0$, the experimental curve reaches its minimum value earlier than the numerical curve, indicating that ΔT_c^{exp} is smaller than $\Delta T_c^{num} = 4.75\,^{\circ}\mathrm{C}$.

As ΔT is increased still further, Marangoni convection becomes more and more important, reducing the relative thermal influence of the walls on the flow. This means that the rotation direction of the vortices at the lateral walls is no longer determined by the wall lateral gradient effect but is essentially dictated by the Marangoni–Bénard instability. When the 1-2 interface is pushing the liquids towards the wall, the colder Fluorinert and the hotter silicone oil move away from that interface. But, $T_2 - T_3$ will now decrease and on the other hand $T_4 - T_5$ will increase so that Δ_2 will increase towards zero and become positive.

This behaviour is well reproduced by both the numerical and the experimental results. Generally, the numerical curve matches quite well the experimental points for $\Delta T < 10\,^{\circ}\mathrm{C}$. Beyond this value of ΔT, the recorded experimental values of Δ_2 are significantly larger than their numerical counterparts indicating that the real flow strength is larger than the simulated one (figure 10). The transition between regime 2 and regime 3 corresponding to the reverse of the rotation of the lateral vortices occurs for $\Delta T^{\mathrm{exp}} = 6.9\,^{\circ}\mathrm{C}$ whereas it occurs for $\Delta T^{\mathrm{num}} = 7.6\,^{\circ}\mathrm{C}$ in the numerical simulations. The agreement for this nonlinear effect thus appears quite good.

4.2. *Flow pattern analysis*

The flow is visualized using a light sheet parallel to the widest side of the experimental cell; it is 1 mm thick and located 10 mm from the front window inside the liquids. The images are digitized and the velocity of the tracer particles is measured using a grey level correlation algorithm. The flow is resolved in $1.2\,\mathrm{mm}^2$ windows. To improve the signal-to-noise ratio and to increase the number of velocity vectors computed, the velocity maps shown here are time averaged. The average velocity vector $\bar{v}(x, y)$ is computed as

$$\bar{v}(x, y) = \frac{1}{N} \sum_{t=t_0}^{t_1} v(t)(x, y),$$

where N is the number of samples acquired between t_0 and t_1, t_0 is the start of the sampling sequence and t_1 the end of the sampling sequence.

4.3. *Onset of convection*

No convection is observed inside the fluid cell for time $t < 850\,\mathrm{s}$ for which the temperature differences imposed across the three layers are smaller than $\Delta T^{\mathrm{exp}} = 3.8\,^{\circ}\mathrm{C}$. An organized flow is observed from $t = 2860\,\mathrm{s}$ ($\Delta T^{\mathrm{exp}} = 4.9\,^{\circ}\mathrm{C}$) onwards. The Marangoni–Bénard instability sets in for $\Delta T_c^{\mathrm{exp}}$ between $3.8\,^{\circ}\mathrm{C}$ and $4.9\,^{\circ}\mathrm{C}$.

4.3.1. *Regime 2*

An organized flow is observed in layers 1 and 2 with two rolls located in the central region of the cell. Layer 3 is at rest (figure 11*a*). In the middle of the cell, as observed in the numerical simulations for regime 2, the flow in layer 1 is rising towards layer 2. Near the lateral walls, the flow seems to be very weak. Actually, for the Marangoni–Bénard instability convection always starts near the lateral walls (Koschmieder 1992). It is very likely that, in that region, the largest components of the velocity vectors are perpendicular to the visualization plane, and thus no measurements were possible. As ΔT^{exp} is increased, four convective rolls become clearly visible in layers 1 and 2 (figure 11*b*).

4.3.2. *Regime 3*

The roll at the right-hand side, initially much larger than the other ones, shrinks progressively (figure 11*c*, *d*). The pattern becomes more regular as the different rolls become of the same size (figure 11*e*). The long exposure time picture given in figure 12 is a visualization of the streamlines in regime 3. While convection is intense in layers 1 and 2, it is very weak in layer 3. At the walls, the direction of rotation is opposite to the one of regime 1 and 2, as the numerical scheme predicts. Near interface 2-3, close to the lateral walls, the two residual vortices are clearly apparent. The characteristic shapes of the central vortices in layer 2 compare very well with the numerical simulations.

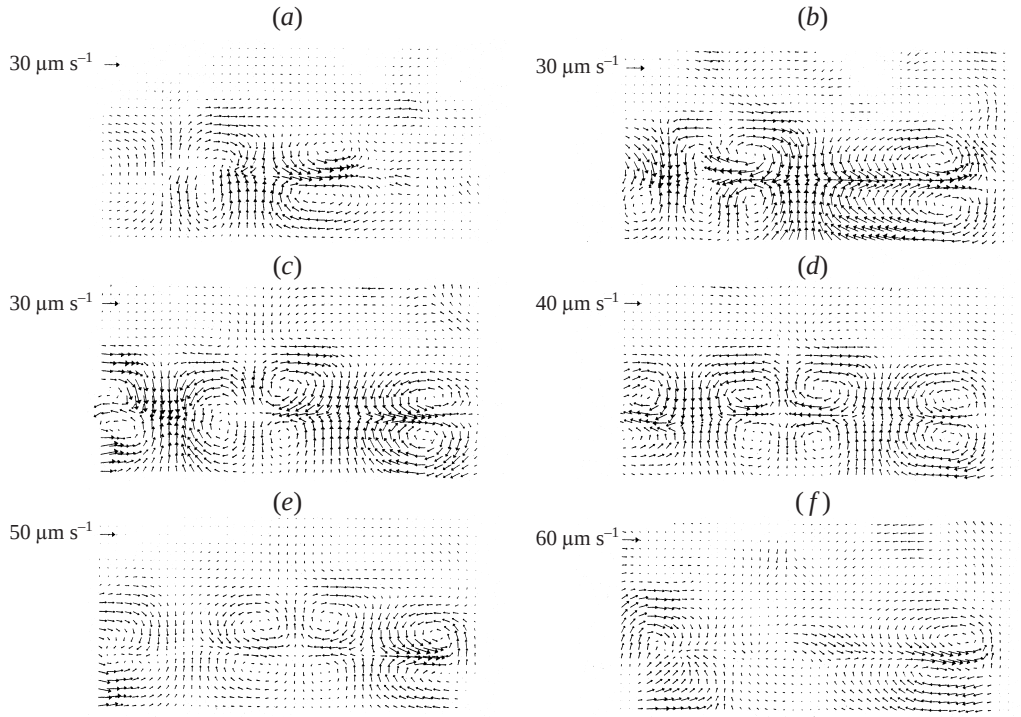

FIGURE 11. Experimental velocity fields, vector scale is given in upper left corner. (*a*) $\Delta T^{exp} = 5.5\,^{\circ}\mathrm{C}$, $v_x(\max) = 44\,\mu\mathrm{m\,s^{-1}}$, $v_y(\max) = 28\,\mu\mathrm{m\,s^{-1}}$. (*b*) $\Delta T^{exp} = 6.7\,^{\circ}\mathrm{C}$, $v_x(\max) = 38\,\mu\mathrm{m\,s^{-1}}$, $v_y(\max) = 34\,\mu\mathrm{m\,s^{-1}}$. (*c*) $\Delta T^{exp} = 7.8\,^{\circ}\mathrm{C}$, $v_x(\max) = 41\,\mu\mathrm{m\,s^{-1}}$, $v_y(\max) = 36\,\mu\mathrm{m\,s^{-1}}$. (*d*) $\Delta T^{exp} = 8.7\,^{\circ}\mathrm{C}$, $v_x(\max) = 57\,\mu\mathrm{m\,s^{-1}}$, $v_y(\max) = 37\,\mu\mathrm{m\,s^{-1}}$. (*e*) $\Delta T^{exp} = 9.7\,^{\circ}\mathrm{C}$, $v_x(\max) = 72\,\mu\mathrm{m\,s^{-1}}$, $v_y(\max) = 43\,\mu\mathrm{m\,s^{-1}}$. (*f*) $\Delta T^{exp} = 12.4\,^{\circ}\mathrm{C}$, $v_x(\max) = 82\,\mu\mathrm{m\,s^{-1}}$, $v_y(\max) = 44\,\mu\mathrm{m\,s^{-1}}$.

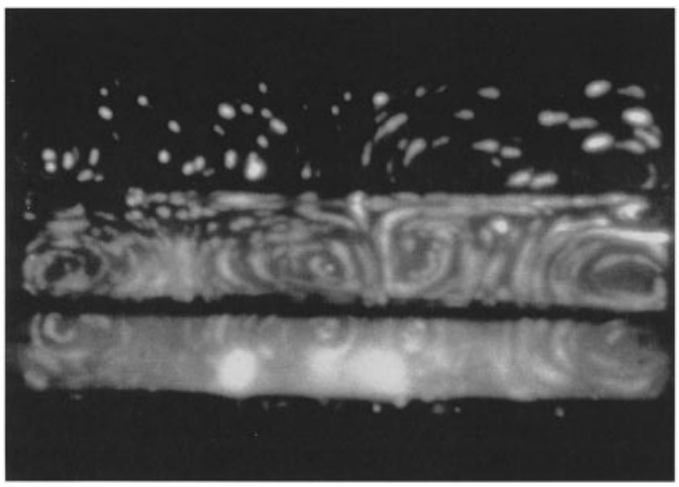

FIGURE 12. Long exposure time picture of the convective flow $\Delta T^{exp} = 9.7\,^{\circ}\mathrm{C}$.

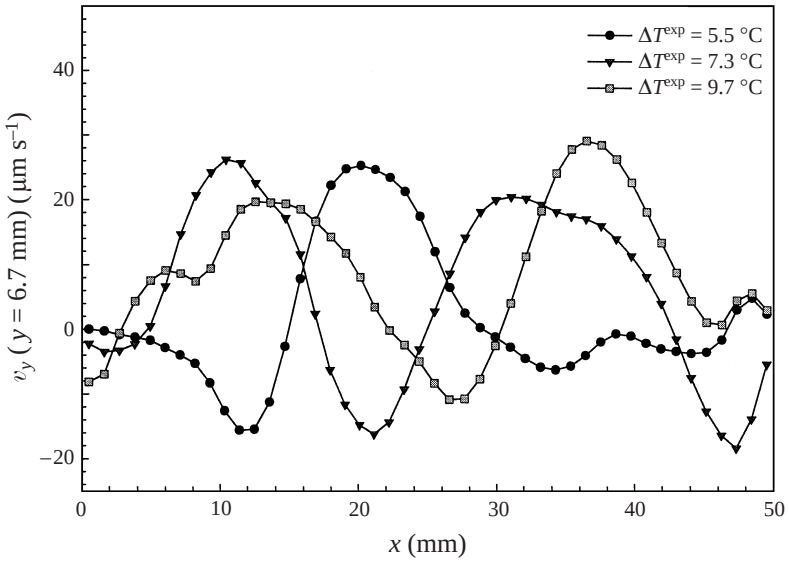

FIGURE 13. Experimental velocity profile v_y in layer 1 at $y = (2/3)h$ plotted vs. x.

As ΔT^{exp} is further increased, the v_z velocity component perpendicular to the light sheet is dominant in the central region of layers 1 and 2 and the structure of the flow cannot be understood using two-dimensional visualization (figure 11*f*). Vortices are however still visible near the lateral walls.

4.3.3. *Velocity profiles*

Corresponding to the numerical results (compare with figure 8), experimental horizontal v_y profiles (taken at $y = (2/3)h$) are shown on figure 13. For the profile that corresponds to regime 2 (circles), the flow is rising up in the centre region and very weak near the walls. The profile is shifted to the left when ΔT^{exp} is increased. The magnitude of the velocity does not increase as ΔT^{exp} is increased. This is probably an artefact due to the three-dimensional nature of the convection cells, the light sheet not necessarily being located exactly in a plane where the z velocity component vanishes.

4.4. *Comparison with the linear stability analysis and the numerical simulations*

4.4.1. *Onset of convection*

Visual observations indicate that convection starts for a temperature difference lying between 3.8 °C and 4.9 °C. The comparison of the thermal data using Δ_2 indicates that the effect of the experiment flow on the thermal field is qualitatively the same as the numerical flow (see figure 10). A careful analysis of Δ_2 also shows that ΔT_c^{exp} is lower than $\Delta T_c^{num} = 4.75\,°C$ but does not permit the uncertainty in ΔT_c^{exp} to be further reduced. Nevertheless, ΔT_c^{exp} is within 20% of ΔT_c^{num} which is quite satisfactory since even in an accurately controlled ground experiment one expects an error of about 10% on the measured Marangoni number (Koschmieder & Biggerstaff 1986).

4.4.2. *Convection*

The experimental results compare well with the results of two-dimensional numerical simulations and the linear stability analysis. The instability is driven by the 1-2

interface in layers 1 and 2 while layer 3 is almost at rest. The number of convection cells (two) is in perfect agreement with the linear stability analysis which predicts that the critical wavelength $\lambda_c = 2\pi/k_c h = 2.56\,\text{cm}$ is half of the length of the container. Both regimes 2 and 3 identified in the numerical results are observed experimentally through the dependence of Δ_2 on ΔT^{exp} and the velocity fields. The inversion of the vortices rotation in the numerical simulations is visible in the experimental pattern: compare figure 11(*a*) and figure 11(*d*). In regime 3, experimental patterns are very similar to the simulated ones. In particular, detailed features of the flow, related to the effect of the lateral walls, are present in both cases (compare figure 5*d* and figure 12).

5. Conclusions

In this paper, the first experimental results on the Marangoni–Bénard instability in a multilayer system are presented. This investigation has been performed in microgravity, where the influence of the Rayleigh mechanism of instability is negligible. A pure thermocapillary-driven phenomenon has thus been analysed. Microgravity permits the mechanical stability of a symmetrical three-layer system (with identical external layers). This configuration allows comparison of the behaviour of physically identical liquid–liquid interfaces which have opposite orientations with respect to the temperature gradient.

The observations confirm the criterion for the onset of convection found by Scriven & Sternling (1959), Smith (1966) and Reichenbach & Linde (1981). A free interface will lead to the onset of convection provided the hotter liquid has a lower thermal diffusivity than the adjacent colder one. This is true for usual couples of liquids whose interfacial tension is a decreasing function of the temperature (or for most liquid–gas systems).

Reasonable quantitative agreement between numerical and experimental results is found for the critical temperature difference for the onset of the Marangoni–Bénard instability and for the spatial wavenumber. There is also qualitative agreement between the values of the velocity fields which were numerically simulated in two dimensions and those that were experimentally measured. However, the modules of the velocity vectors computed by numerical simulation are about half of the measured ones.

Direct simulation of the three-dimensional flow in a symmetrical three-layer system could provide a better quantitative agreement but would require larger computer resources. Significant reduction of the computing cost could however be achieved by computing the Stokes equation instead of the Navier–Stokes equation (Bestehorn 1995 and Thess, Spirn & Jüttner 1995) provided that the Reynolds number is small enough. Another possibility is to assume that the flow pattern is symmetrical with respect to the vertical axis for example.

Another question that remains to be answered is what is responsible for the direction of the flow along the wall when one reaches the transition zone between regime 2 and 3.

We are grateful to the European Space Agency and its Prodex Programme for their support in the preparation of the microgravity experiment whose results are presented here. We wish to thank Dr T. Roesgen and M. R. Totaro from ESA/ESTEC for the help they provided in the velocity field analysis with the PIV software. We also would like to thank Dr B. Roux, Dr Q. S. Liu and Dr P. Colinet for fruitful discussions related to thermocapillary flows in multilayer systems.

This text presents research results of the Belgian Programme on Interuniversity Poles

of Attraction (PAI 04-6) initiated by the Belgian State Federal Office of Scientific Technical and Cultural Affairs. The scientific responsibility is assumed by its authors.

REFERENCES

Bestehorn, M. 1995 Phase and amplitude instabilities for Bénard–Marangoni convection in fluid layers with large aspect ratio. *Phys. Rev.* E **48**, 3622–3634.

Block, M. J. 1956 Surface tension as the cause of the Bénard cells and surface deformation in a liquid film. *Nature* **178**, 650–651.

Burkersroda, C., Prakash, A. & Koster, J. 1994 Interfacial tension between fluorinert and silicone oils. *Microgravity Q.* **4** (2), 93–99.

Cardin, Ph., Nataf, H.-C. & Dewost, Ph. 1991 Thermal coupling in layered convection: evidence for an interface viscosity control from mechanical experiments and marginal stability analysis. *J. Phys. Paris* II **6**, 599–622.

Chandrasekhar, S. 1961 *Hydrodynamic and Hydromagnetic Stability*. Oxford University Press.

Dauby, P. C. & Lebon, G. 1996 Bénard–Marangoni instability in rigid rectangular containers. *J. Fluid Mech.* **329**, 25–64.

Drazin, P. G. 1992 *Nonlinear Systems*, Cambridge University Press.

Géoris, Ph., Hennenberg, M., Simanovskii, I. B., Nepomniashchy, A., Wertgeim, I. & Legros, J. C. 1993 Thermocapillary convection in a multilayer. *Phys. Fluids* A **5**, 1575–1582.

Harkins, W. D. 1952 *The Physical Chemistry of Films*. Reinhold.

Imaishi, N. & Fujinawa, K. 1974 Thermal instability in two fluid layers. *J. Chem. Engng Japan* **7**, 87–92.

Koschmieder, E. L. 1992 *Bénard Cells and Taylor Vortices*. Cambridge University Press.

Koschmieder, E. L. & Biggerstaff, M. I. 1986 Onset of surface tension driven Bénard convection. *J. Fluid Mech.* **167**, 49–64.

Manneville, P. 1991 *Structures Dissipatives Chaos et Turbulence*. Aléa Saclay.

Pearson, J. R. 1958 On convection cells induced by surface tension. *J. Fluid Mech.* **4**, 489–500.

Peyret, R. & Taylor, D. 1990 *Computational Methods for Fluid Flow*. Springer.

Rasenat, S., Busse, F. H. & Rehberg, I. 1989 A theoretical and experimental study of double-layer convection. *J. Fluid Mech.* **199**, 519–540.

Reichenbach J. R. & Linde, H. 1981 Linear perturbation analysis of surface tension driven convection at a plane interface (Marangoni instability). *J. Interface Colloid Sci.* **81**, 433–443.

Scriven L. E. & Sternling, C. V. 1959 Interfacial turbulence: hydrodynamic instability and the Marangoni effect. *AIChE J.* **6**, 514–523.

Scriven, L. E. & Sternling, C. V. 1964 On cellular convection driven by surface tension gradients: effects of mean surface tension and surface viscosity. *J. Fluid Mech.* **19**, 321–340.

Simanovskii, I. B. & Nepomniashchy A. A. 1993 *Convective Instabilities in Systems with Interface*. Gordon and Breach.

Smith, K. A. 1996 On convective instability induced by surface tension gradients. *J. Fluid Mech.* **24**, 401–414.

Takashima, M. 1981 Surface tension driven instability in a horizontal liquid layer with a deformable free surface I. Stationary convection. *J. Phys. Soc. Japan* **50**, 2745–2750.

Thess, A., Spirn, D. & Jüttner, B. 1995 Viscous flow at infinite Marangoni number. *Phys. Rev. Lett.* **75**, 4614–4617.

Wahal, S. & Bose, A. 1988 Rayleigh–Bénard and interfacial instabilities in two immiscible liquid layers. *Phys. Fluids* **31**, 3502–3510.

Zeren, W. & Reynolds, W. 1972 Thermal instabilities in two-fluid horizontal layers. *J. Fluid Mech.* **53**, 305–327.